Journal of Solid State Chemistry xxx (xxxx) xxx-xxx

Contents lists available at ScienceDirect

Journal of Solid State Chemistry

journal homepage: http://ees.elsevier.com

Effective strategy to coupling Zr-MOF/ZnO: Synthesis, morphology and photoelectrochemical properties evaluation

Letícia G. da Trindade [a,**], Katiúscia M.N. Borba [b], Aline B. Trench [c], Letícia Zanchet [b], Vinícius Teodoro [c], Fenelon M.L. Pontes [a], Elson Longo [c], Tatiana M. Mazzo [d,*]

[a] Department of Chemistry, Universidade Estadual Paulista - Unesp, P.O. Box 473, Bauru, SP, 17033-360, Brazil
[b] LRC - Institute of Chemistry, Universidade Federal do Rio Grande do Sul - UFRGS, P.O. Box 15003, Porto Alegre, RS, 91501-970, Brazil
[c] LIEC – CDMF - Department of Chemistry, Universidade Federal de São Carlos - UFSCar, P.O. Box 676, São Carlos, SP, 13565-905, Brazil
[d] Institute of Marine Sciences, Universidade Federal de São Paulo - UNIFESP, Santos, SP, 11070-102, Brazil

ARTICLE INFO

Keywords
ZnO
Zr-MOF
Metal-organic framework
Photoanode
Solar cell

ABSTRACT

Zr-MOF was coupled with ZnO particles by mechanical mixture followed by heat treatment at 400 °C. The Zr-MOF influence on the ZnO structure was investigated by means of X-ray diffraction (XRD), surface area analysis (BET), electron microscopy (SEM and TEM), spectroscopy (XPS) and photoelectrochemical experiment. The main phase of the synthesized samples well matched the hexagonal wurtzite structure of ZnO. The XPS analysis confirm the heterostructure formation between ZnO and Zr-MOF materials and shows that the sample with 25 wt% Zr-MOF (ZnO/MOF25) has the higher proportion of lattice oxygen compared to the pristine ZnO and the sample with 50 wt% Zr-MOF (ZnO/MOF50). The reduction in the oxygen vacancies in the ZnO/MOF25 sample supports the greater effectiveness of heterostructure formation in this sample. The results also indicated that the ZnO/MOF25 sample is a promising photoelectrode for solar cells.

1. Introduction

As the population increases, there is also an increasing demand for energy, which is mostly supplied by fossil fuels [1]. The use of non-renewable energy sources leads to a growing concern about an eminent energy crisis [2]. In the current world scenario, sustainability can be defined as the search for balance between the use of natural resources and the production of energy in a safe and accessible way. Therefore, it is crucial to conduct some research on the development of new forms of energy generation using sustainable energy technologies, consequently avoiding the exhaustion of current energy sources and reducing environmental problems [3–6].

Renewable energy-based technologies include the use of solar energy, an abundant and available energy source in the planet. Among the various technologies that convert incident solar radiation into electricity, the dye-sensitized solar cells (DSSCs) stand out due to their low cost and simple manufacturing method [7–10]. DSSCs are classified as the third generation of solar cells and consist of a conducting glass substrate, a dye-sensitized metal oxide semiconductor photoanode, a catalyst counter electrode and an electrolyte solution inserted between the two electrodes [11,12]. However, such devices have low power conversion efficiency (PCE), which represents a barrier to the use of these devices in the photovoltaic market [13,14]. The low PCE is related to the electronic, morphological and optical properties of the materials used as photoanodes.

Currently, ZnO has been used as an alternative material to TiO_2 for perovskite solar cells (PSCs) and DSSCs. PSCs with ZnO can have high PCE, since, it has an energy band structure and physical properties similar to those of TiO_2 [15]. For being a metal oxide and semiconductor and having a large direct band gap (3.37 V) [16], besides exhibiting electron mobility and electron diffusion coefficient higher than that of TiO_2 [17]. Another advantage of ZnO is that it can be easily processed in solution at low temperatures to produce structures with different morphologies [18]. Recent researches, chosen ZnO nanoparticles as additive in perovskite materials like $CsPbBr_3$/ZnO thin films [19], $CsPbIBr_2$ improved by introducing NH_4Cl-modified ZnO [20], $CsPbIBr_2$ employing ZnO as electron transporting layer (ETL) [21], $CsPbBr_3$ using ZnO nanorods as ETL [22], among others.

ZnO is also an excellent candidate for the production of photoanodes in DSSCs devices. However, the DSSC performance is affected by the ZnO morphology and the electrode thickness. To increase the performance of this device, research has been carried out aiming to modify the morphology and thickness of ZnO [23–25].

Recently, metal-organic frameworks (MOFs) have received considerable attention with respect to their photocatalytic and photovoltaic applications due to their distinct properties, such as tunable porosity and

* Corresponding author.
** Corresponding author.
E-mail addresses: lgt.gtrindade@gmail.com (L.G. da Trindade); tatimazzo@gmail.com (T.M. Mazzo)

https://doi.org/10.1016/j.jssc.2020.121794
Received 10 August 2020; Received in revised form 3 October 2020; Accepted 14 October 2020
Available online xxx
0022-4596/

long-distance internal energy migration pathways [26–28]. MOFs are hybrid materials constructed by the combination of organic binders and inorganic nodes [29]. In addition, their use in DSSCs can minimize the charge recombination losses and may allow the use of a wider solar spectrum for light collection [30].

Dou et al. [31] prepared pure anatase TiO_2 using MOF MIL-125 (Ti) as a precursor for a DSSC photoanode. The DSSC made with the TiO_2 obtained by the calcination of MIL-125 (Ti) at 380 °C for 5 h in air showed an efficiency of 7.20%. This good energy conversion efficiency was attributed to better dye adsorption, faster electron transport and improved charge collection efficiency.

Lee et al. [32] used two types of Zr-MOFs, UiO-66 and MOF-808, to modify the crystallinity of perovskite film. They demonstrated that solar cells of perovskite (PVSCs) modified using UiO-66/MOF-808 achieve energy conversion efficiencies (PCEs) of 17.01% and 16.55%, surpassing the PVSC without MOF (15.79%). This improvement can be associated with the fact that while UiO-66/MOF-808 serve as interlayer in conjunction with the perovskite film, they have the UV-filtering ability and the capability to increase the perovskite crystallinity.

Considering the discussion above, the expected advantages of the combination of ZnO and Zr-MOF encouraged us to exploit such composites in order to develop a photoanode for possible application in solar cells. There are not many studies that report the use of the ZnO/Zr-MOF composite for application in DSSCs photoelectrodes. We report here a simple, low cost and reproducible manufacturing route of these materials. The pure ZnO and ZnO/Zr-MOF composites had their key properties such X-ray diffraction, morphology, photoluminescence and photoelectrochemical comparatively studied.

2. Materials and methods

2.1. Synthesis of ZnO and Zr-MOF

The ZnO nanoparticles were obtained through chemical precipitation method in aqueous media at room temperature by modification of the synthesis realized by our group [33,34]. In a typical process 50 mL of KOH solution (2.0 mol L^{-1}) (Sigma-Aldrich) was added in 50 mL of $Zn(NO_3)_2{\cdot}6H_2O$ solution (0.3 mol L^{-1}) (99%, Sigma-Aldrich) under constant stirring during 20 min. The resultant particles were separated by centrifugation and washed several times with deionized water at pH 7. Finally, the samples were oven-dried for 12 h at 60 °C.

The synthesis of the Zr-MOF was performed as described in the literature [35,36]. The reagents were mixed in the proportion $ZrCl_4$:C_6H_4-1,4-$(CO_2H)_2$:2.5 $HCON(CH_3)_2$ and after being solubilized they were added in the autoclave. The reaction was kept in an oven at 125 °C for 24 h; as a result crystals were obtained which then passed through the centrifugation and drying procedures. The crystals were then washed with methanol and dried in an oven until completely purified.

2.2. Electrode preparation

The ZnO, ZnO/MOF25 and ZnO/MOF50 electrodes were prepared according the procedure reported in the literature [33]. Viscous pastes of these materials were prepared by mixing either ZnO (0.0125 g) with ethanol (200 μL) or ZnO (0.0125 g) with Zr-MOF (25 or 50 wt%) in ethanol (200 μL). The mixture was sonicated for 30 min, and after the addition of 60 μL of deionized water, it was sonicated again for another 30 min. The obtained suspensions were applied onto FTO (fluorine-doped tin oxide) substrates using a micropipette in an area of 1 cm^2. The films were then allowed to dry at ambient temperature for 1 h, and then calcined at 400 °C for 1 h, at heating and cooling rates of 0.1 °C min^{-1}, in order to avoid cracking of the film.

2.3. Characterization

The X-ray diffraction (XRD) was measured on a Rigaku detector (CuKα, λ = 0.15406 nm) with a scan rate of 5° min^{-1}. The Brunauer–Emmett–Teller (BET) surface area measurements were performed with Micromeritics TriStar II 3020. Fourier-transform infrared spectroscopy (FTIR) was performed on a Bruker EQUINOX 55 spectrometer. The thermal stability of the samples was determined by TG analysis using a TA Instruments Q-50 apparatus in the temperature range of 20–700 °C at a heating rate of 10 °C min^{-1} under N_2 atmosphere. The Raman spectra were recorded at room temperature using a triple grating JobinYvon T64000 spectrometer equipped with a liquid N2-cooled charge-coupled device (CCD). The samples were analyzed by FEG-SEM using a ZEISS model 105 DSM940A instrument working at 10 keV, and a FEI Tecnai F20 transmission electron microscope (TEM) operating at 200 keV equipped with an energy dispersive X-ray spectrometer (EDS). The UV–vis spectra were recorded by a Cary 5 G (Varian) apparatus with a wavelength range of 250–800 nm. X-ray photoelectron spectroscopy measurements were carried in a Scienta Omicron ESCA + (Germany) spectroscope with monochromatic Al Kα radiation (1486.7 eV). The binding energies of all elements were calibrated by referencing to the C 1*s* peak at 284.8 eV. The photoluminescence (PL) characterization was obtained at room temperature using a Thermal Jarrel-Ash Monospec 27 cm monochromator and a Hamamatsu R955 photomultiplier under 350.7 nm (3.54 eV) excitation. The photoelectrochemical performances were tested by using three-electrode cell with a quartz glass window where the prepared samples, Pt wire and Ag/AgCl electrode have been used as working, counter and reference electrodes, respectively. The electrolyte was acetonitrile solution with 10 mM LiI, 1 mM I_2, and 0.1 M $LiClO_4$. The current density-voltage (J-V) curves of the samples have been analyzed using an Autolab PGSTAT302 N potentiostat. The J-V curves have been evaluated for both illuminated and dark conditions using a Newport Sol3A Class AAA solar simulator with a 100 W Xenon lamp.

3. Results and discussion

Fig. 1 shows the XRD patterns of the pure ZnO, Zr-MOF and ZnO/MOF25 and ZnO/MOF50 composite samples. All evident diffraction peaks observed in the ZnO sample were indexed as hexagonal wurtzite structure (JCPDS Data Card No. 36–1451) for the pure ZnO phase with $P6_3mc$ space group, which is in agreement with the data reported in the literature [33]. The diffraction peaks observed in the Zr-MOF sample demonstrated its successful preparation since the results are congruent with previous publications [37]. After the mixture of ZnO and Zr-MOF, all the main diffraction peaks in the ZnO/MOF samples still corresponded to the hexagonal wurtzite structure of ZnO, indicating that the addition of Zr-MOF did not change the crystal structure of the particle. Fig. 1 (b) introduce a expand view of the diffraction peaks of the (111), (002), (022), (113) and (222) planes of Zr-MOF for all samples. We can observed that the ZnO/MOF 25 and ZnO/MOF50 samples showed the diffraction peaks related to Zr-MOF and the planes were shifted to low angles. Fig. 1 (c) brings a magnified view of the diffraction peaks of the (110), (002) and (101) planes of ZnO for all samples. It can be noted that with the addition of different amounts of Zr-MOF the (110), (002) and (101) planes significantly shifted to higher angles. This behavior can be explained by the fact that a solid-solid interface between two materials in a heterojunction with different crystal structures and lattice parameters can results in lattice mismatch in the interface. This lattice mismatch generates an interfacial strain that results in structural distortions. These distortions at the interface are responsible for the generation and propagation of lattice distortions along the particle of strained material [38]. Therefore, the lattice contraction of the ZnO structure in the composite samples supports the effective formation of the heterostructure in these samples.

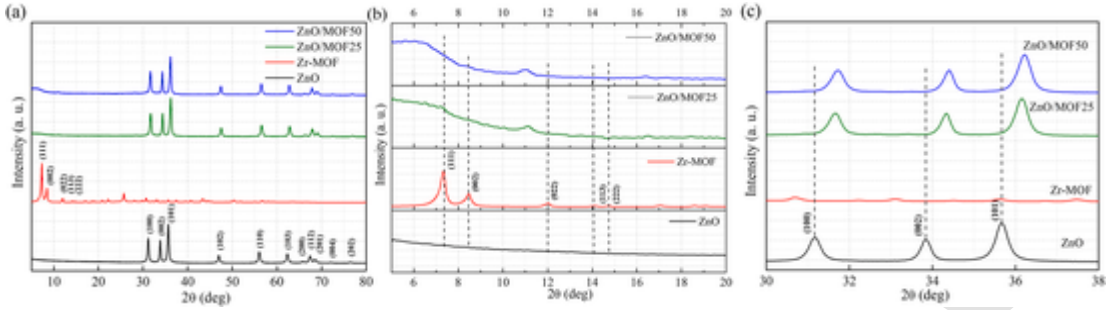

Fig. 1. XRD patterns of ZnO, Zr-MOF, ZnO/MOF25 and ZnO/MOF50 (a) and the enlarged diffraction peaks from 5° to 20° (b) and 30°–38° (c).

Fig. 2 (a) shows the ATR-FTIR of the ZnO, Zr-MOF and ZnO/MOF25 and ZnO/MOF50 composite samples. From the ZnO spectrum, it is possible to see bands at 860 and 570 cm^{-1} assigned to characteristic absorption peaks of the Zn–O bond, suggesting the formation of ZnO particles [39]. The bands at 1570 and 1390 cm^{-1} are attributed to symmetric and asymmetric stretching vibration of the *N*–O group of nitrate, indicating the presence of nitrate anionic moieties on the ZnO surface. Finally, the weak broad band around 3460 cm^{-1} is due to the O–H stretching vibration. Regarding the Zr-MOF spectrum, the bands observed at 1590 and 1404 cm^{-1} are attributed to the O–C–O asymmetric and symmetric stretching in the terephthalic acid ligand. The bands at 754 and 668 cm^{-1} correspond to the O–H and C–H vibrations in the terephthalic acid ligand [40]. When Zr-MOF was incorporated into the ZnO particles, in addition to the pure oxide characteristic bands we could also observe the appearance of two bands at 1590 and 1404 cm^{-1}, which correspond to the O–C–O stretching in the terephthalic acid ligand of the Zr-MOF for both ZnO/MOF composites. This result clearly shows that the composite was formed at both Zr-MOF concentrations used (25 and 50 wt%).

The specific surface areas of ZnO, Zr-MOF and ZnO/Zr-MOF samples were studied by N_2 adsorption-desorption isotherms, which are displayed in Fig. 2 (b). The N_2 adsorption-desorption curves of the samples are all Type II isotherms, and their specific surface areas were calculated by the BET method (Table 1). Although all materials exhibited a high surface area, the highest was observed in the Zr-MOF sample, 986.5 $m^2\ g^{-1}$, which was approximately equal than that found in the literature to UiO-66, 1067 $m^2\ g^{-1}$ [41]. The BET surfaces of the ZnO/Zr-MOF samples also increased as a function of Zr-MOF content (from 50.9 to 60.4 $m^2\ g^{-1}$). This increase can be related to morphological changes caused by the ZnO/MOF heterostructure formation.

Fig. 2 (c) displays the TG and DTG analyses of all samples. The TGA curve of the pure ZnO shows that the oxide is stable up to 700 °C, exhibiting a mass loss of only 2%. This can be attributed to the loss of adsorbed substances on the oxide surface. On the other hand, the TGA curve demonstrates that the Zr-MOF is stable up to 500 °C with a mass loss of 32%, which occurred in three stages: the first one at 76 °C is attributed to the initial solvent loss; the second weight loss detected in the range of 150–500 °C is related to the dehydration of $Zr_6O_4(OH)_4$ nodes to Zr_6O_6; and finally the last stage at 610 °C corresponds to the decomposition of the organic linkers [42]. Both composite samples (ZnO/MOF25 and ZnO/MOF50) exhibited the same behavior and presented a mass loss of 8%. The loss observed in the range of 460–545 °C can be attributed to the dehydration of $Zr_6O_4(OH)_4$ nodes to Zr_6O_6, indicating that Zr-MOF was successfully incorporated into the oxide.

Fig. 3 shows the Raman peaks of the ZnO, Zr-MOF and ZnO/MOF25 and ZnO/MOF50 composite samples. The peaks observed in the ZnO sample at 212 and 325 cm^{-1} are assigned to the acoustic phonon overtone and optical phonon overtone with A_1 symmetry, respectively [43]. The peak at 340 cm^{-1} corresponds to the multiphonon E_2 high mode (E_{2H}) [44], while that at 432 cm^{-1} is attributed to the E_1 transverse optical (TO) and E_{2H} modes [43]. Longitudinal optical phonon vibration with A_1 and E_1 symmetries (A_1 LO and E_1 LO) can be observed around 575 cm^{-1} [45]. The broad band between 1080 and 1115 cm^{-1} is assigned to the acoustic combination of A_1 (TO), E_1 (TO) and E_2 low modes (E_{2L}) [46]. The Raman peaks of the Zr-MOF sample above 800 cm^{-1} are those involving the organic ligands, which vibrate freely in the framework cages. The high frequency peak at 1600 cm^{-1} is in fact a combination of one A_g, two E_g, and three F_{2g} modes, with comparable intensities [47]. When 25 wt% Zr-MOF (ZnO/MOF25 sample) was added to ZnO, some ZnO vibration modes seemed more intense and shifted to lower values, while the corresponding Zr-MOF vibration modes appeared with low intensity. On the other hand, when the amount of Zr-MOF was increased to 50 wt% (ZnO/MOF50 sample), there was a decrease in the intensity of ZnO vibrational modes and a predominance of Zr-MOF vibrational modes.

Fig. 4 shows the FEG-SEM images of the pure ZnO, pure Zr-MOF and ZnO/MOF25 and ZnO/MOF50 composite samples. It can be observed that the ZnO sample (Fig. 4 (a)) exhibited a flower-type structure consisting of "micro-petals", which was already reported in the literature [33,48], while the Zr-MOF sample (Fig. 4(b)) presented a morphology with irregularly cubes, which is one of typical shape of the Zr-MOF [49]. However, the addition of different amounts of Zr-MOF completely changed the ZnO morphology (Fig. 4 (c) and (d)), suggesting that Zr-MOF plays a vital role in the size and morphology of ZnO particles. When Zr-MOF was added, the flower-type structure was minimized and tightly interconnected with each other to form cross-linked multileveled porous blocks. Based on the FEG-SEM analysis, the size of

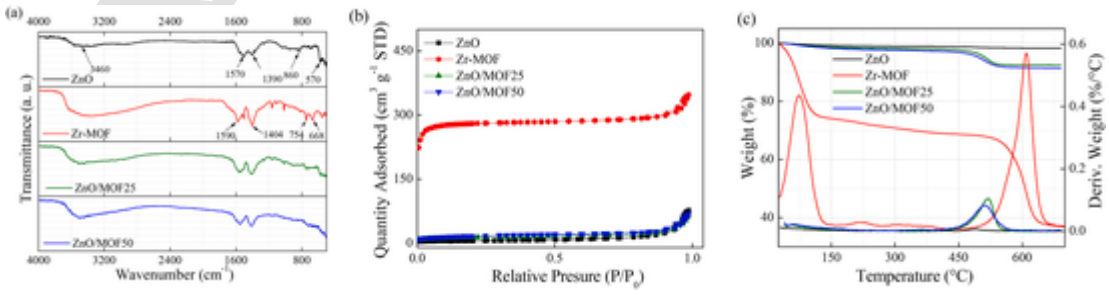

Fig. 2. ATR-FTIR spectra (a) typical N_2 adsorption–desorption isotherm (b) and TG and DTG analysis (c) of ZnO, Zr-MOF, ZnO/MOF25 and ZnO/MOF50.

Table 1
Surface area, pore diameter and average particle size of ZnO, Zr-MOF, ZnO/MOF25 and ZnO/MOF50 samples.

Sample	BET		FEG-SEM Average particle size (μm)
	Surface area (m^2 g^{-1})	Pore diameter (nm)	
ZnO	22.3	19.6	0.889
Zr-MOF	986.5	10.6	0.097
ZnO/MOF25	50.9	12.6	0.179
ZnO/MOF50	60.4	18.5	0.130

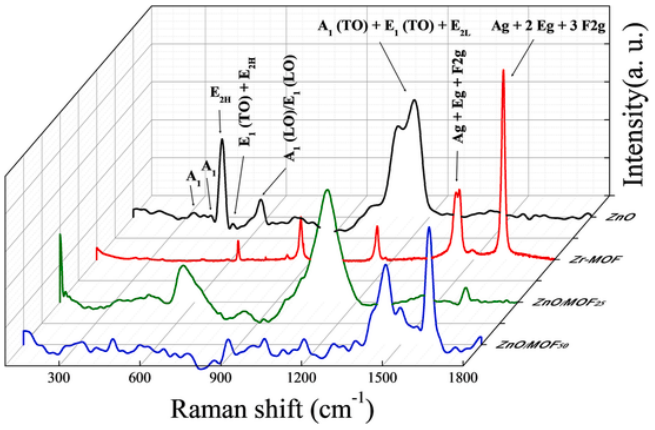

Fig. 3. Raman spectra of ZnO, Zr-MOF, ZnO/MOF25 and ZnO/MOF50.

the ZnO particles decreased with the insertion of Zr-MOF. Therefore, the morphological evolution of ZnO from flower-type structure to cross-linked multileveled porous nanoflowers was mainly associated with the addition of Zr-MOF during the preparation of the samples.

Fig. 5 shows the TEM images of the ZnO and ZnO/MOF samples with the EDS spectra of the selected regions for comparison. As shown in Fig. 5 (a), the pristine ZnO had a flower-type structure. When 25 wt% Zr-MOF was added, the sample exhibited the same shape as the pure ZnO, as seen in Fig. 5 (b). When the Zr-MOF concentration was increased to 50 wt% (Fig. 5 (c)), each nanoflower in the sample became much smaller and closely interconnected to form mesopores. The EDS spectra shows that the Zr element detected increased with the increase of the Zr-MOF content, confirming that such element exists on the surface of ZnO.

The optical band gap of all samples were obtained by UV–Vis spectroscopic measurements. The band gap energies (E_g, eV) of the samples were calculated from their UV–Vis data using the Kubelka–Munk method [16] as follows:

$$\alpha h\nu = A\,(h\nu - E_g)^n \quad (1)$$

where α is the linear absorption coefficient of the material, $h\nu$ is the incident photon energy, A is a proportionality constant related to the material, E_g is the band gap energy of the semiconductor, and n is a constant dependent on the type of electronic transitions. For direct band gap materials, which is the case of ZnO and Zr-MOF, the value of n is 1/2 [50,51]. The direct E_g of the samples are shown in Fig. 6.

The band gap values of the materials studied are 3.22, 3.86, 3.18 and 3.15 eV for the pure ZnO, pure Zr-MOF, ZnO/MOF25 and ZnO/MOF50 samples, respectively. The addition of Zr-MOF caused a small reduction in the band gap value of the composites when compared to that obtained for the pure ZnO. The band gap reduction depends on factors like particle size, optical properties and surface morphology, which influence the penetration of light photons [52]. When the Zr-MOF was incorporated in the ZnO particles, a hierarchical porous structure was formed. This porous structure, combined with the formation of smaller particles, makes the ZnO/MOF material surface rough. These rough surfaces are beneficial because they allow light photons to penetrate deeper into the pores, reflecting multiple times and not easily escaping out [52,53]. Thus, the duration of the light photon stay in these porous surfaces is relatively high. The rate of loss of incident photon scattering on the rough surface is minimum, so the light absorption is increased, and consequently the band gap decreases. On the other hand, at the electronic level, when ZnO/MOF heterostructure is formed, there may be trap-formation, and consequently charges carrier mobility is reduced. As a result, the composite structure will have a new band gap, i.e. the band gap narrows [53].

XPS measurements were carried out in order to understand the chemical composition and structure of the surface of all prepared samples. Fig. 7(a–c) and Fig. 7(e–g) shows the peak-differentiating-imitating analysis of Zn 2*p* and Zr 3*d* high-resolution XPS spectra, respectively, which were performed in CasaXPS software. The Zn 2*p* spectra for ZnO, ZnO/MOF25 and ZnO/MOF50 samples indicated the two components characteristic of spin-orbit coupling, which are related to Zn $2p_{1/2}$ and Zn $2p_{3/2}$ states. The energy splitting (Δ) of Zn 2*p* for all these samples are 23.0 eV, that corresponds to the Zn^{2+} oxidation state in the ZnO structure [55]. The Zr 3*d* spectra for Zr-MOF, ZnO/MOF25 and ZnO/MOF50 samples indicated the two characteristic spin-orbit coupling components related to the Zr $3d_{3/2}$ and Zr $3d_{5/2}$ states, presenting $\Delta = 2.37$ eV, which is assigned to the Zr^{4+} oxidation state in the Zr-MOF structure [56].

Although the samples presented the same oxidation states for Zn^{2+} and Zr^{4+}, energy peak shifts were observed between the samples. Fig. 7 (d) shows the energy values of Zn $2p_{3/2}$ and Zr $3d_{5/2}$ for the prepared samples. As can be seen, the energy values for Zn $2p_{3/2}$ increase in the composite samples in relation to the pristine ZnO, and an opposite behavior was observed for Zr $3d_{5/2}$, which the energy values decrease in the composite samples in relation to the pristine Zr-MOF sample. Once a heterostructure is formed between two materials, a solid-solid interface is formed leading to the band alignment of both structures for the Fermi level alignment. These observed opposite changes in energy values for ZnO and Zr-MOF states are ascribed to the band alignment in the band offset of the ZnO/Zr-MOF heterostructure. Therefore, XPS analysis supports the effective formation of the heterostructure between ZnO and Zr-MOF materials. Besides that, despite both composite samples had lower Zr $3d_{5/2}$ energy values compared to pristine Zr-MOF, the ZnO/MOF25 sample has the lowest value compared to the others. Herewith, this sample presented the greatest effectiveness band alignment, thus resulting in a higher charge carrier transfer in the interface of ZnO/Zr-MOF heterostructure. The lower amount of Zr-MOF in the ZnO/MOF25 compared to the ZnO/MOF50 sample result in a greater dispersion of the Zr-MOF along the ZnO particles, possible increasing the contact area between both materials and hence a greater effectiveness in the band alignment.

Fig. 8 shows the peak-differentiating-imitating analysis of O 1*s* spectra for all prepared samples. The spectra were deconvoluted into three components at approximately 530 eV, 531.5 eV and 533 eV, which are assigned to the lattice oxygen, oxygen vacancies and hydroxyl surface-bound groups. As can be seen, the O 1*s* of Zr-MOF is composed only by the lattice oxygen due to the well-defined organic framework structure. In addition, the O 1*s* of ZnO/MOF25 sample has the higher proportion of lattice oxygen compared to the pristine ZnO and the ZnO/MOF50 samples. Since the surface of pristine ZnO is rich in oxygen vacancies, the decrease in this proportion in ZnO/MOF25 sample supports the greater effectiveness of heterostructure formation in this sample, once the surface oxygen vacancies in ZnO particles were partially electronically filled by the Zr-MOF surface structure to form the solid-solid interface.

The processes of separation and transfer of photoinduced carriers can be understood from the alignment of the energy band for the ZnO/

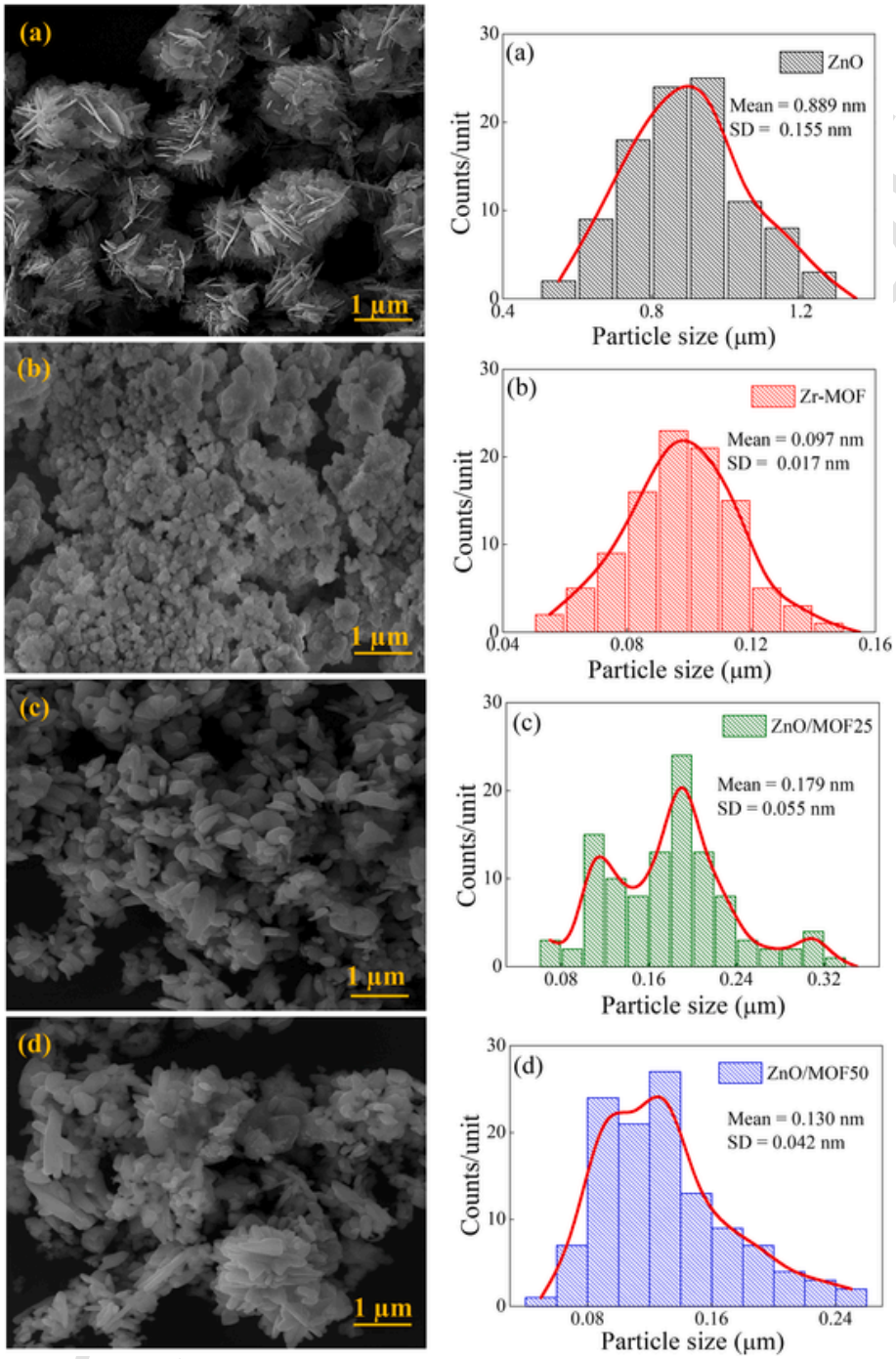

Fig. 4. FEG-SEM images and average particle size of ZnO (a), Zr-MOF (b), ZnO/MOF25 (c) and ZnO/MOF50 (d).

MOF heterojunction. The valence band offset at the heterojunction interfaces can be determined by valence band XPS (VB-XPS), according to Fig. 9 (a).

As shown in Fig. 9 (a), the VB-XPS spectra exhibited the valence band (Ev) of 1.98 eV and 2.20 eV for Zr-MOF and ZnO, respectively. Through E_g values of ZnO and Zr-MOF (3.22 eV and 3.86 eV, respectively), the conduction band (E_c) was obtained of $E_c = E_v - E_g$ and is −1.88 eV and −0.02 eV for Zr-MOF and ZnO, respectively [57]. From these results, we proposed a schematic diagram for energy bands for the ZnO/MOF composite (Fig. 9 (b)). The experimental band gap values of ZnO and Zr-MOF are 3.22 eV and 3.86 eV (Fig. 6), respectively. These band gap values make them active only when exposed to UV light [58]. On the other hand, when Zr-MOF was coupled with ZnO the separation of the photoinduced charge carries are improved. As ZnO and Zr-MOF are typically n-type semiconductors [59,60], this improvement can be attributed to the formation of an n–n semiconductor heterojunction between these materials. Fig. 9 (b) display that when the ZnO/MOF sample was exposed to visible light, the photogenerated electrons (e^-) in the Zr-MOF conduction band (CB) migrated to ZnO, while the holes (h^+) remained in the Zr-MOF valence band (VB), resulting in the separation of the charge carriers.

The VB XPS spectra of the ZnO/MOF25 and ZnO/MOF50 are shown in Fig. 10. They exhibited that the E_v are 2.72 eV and 1.81 eV for the composite with 25 and 50 wt% of Zr-MOF. The E_c are −0.46 eV and −1.31 eV for ZnO/MOF25 and ZnO/MOF50, respectively.

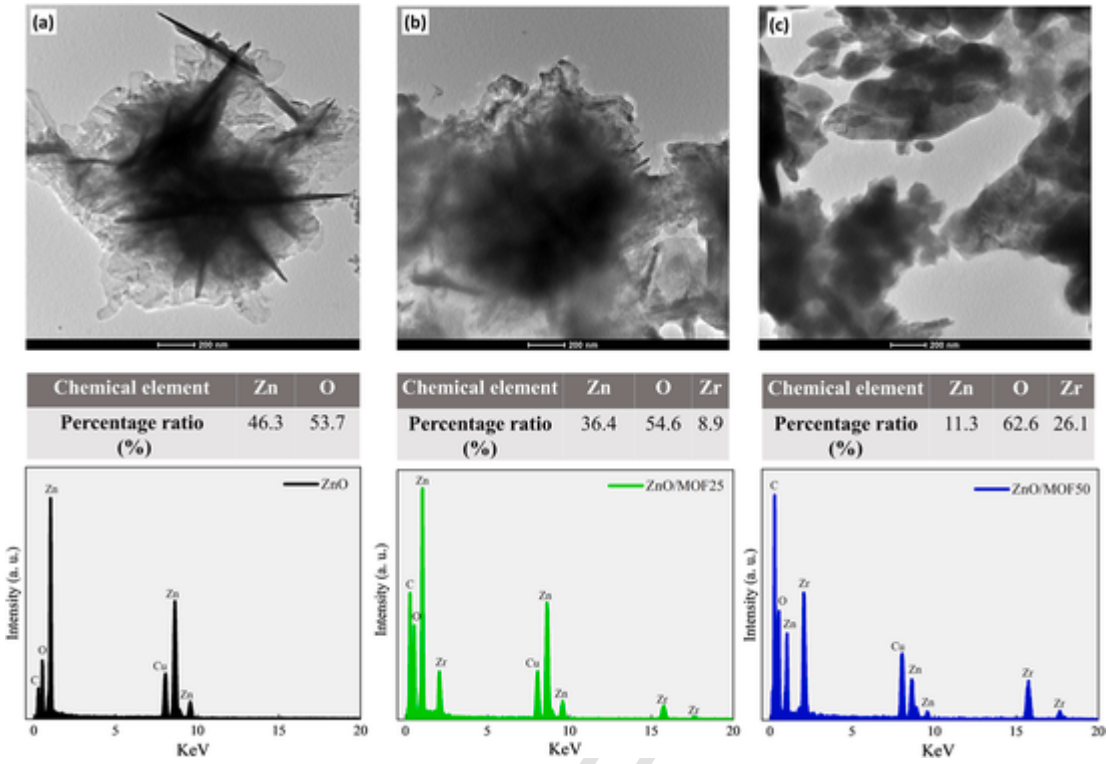

Fig. 5. Transmission electron microscopy (TEM) images and Energy-dispersive X-ray spectroscopy of pristine ZnO (a), ZnO/MOF25 (b), and ZnO/MOF50 (c).

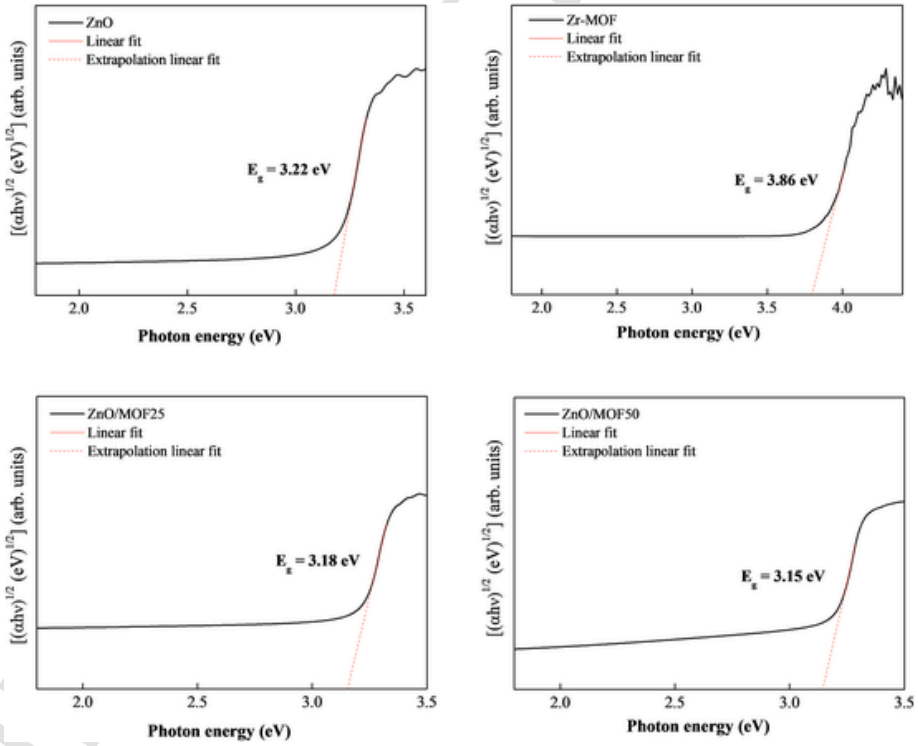

Fig. 6. Tauc plot of ZnO, Zr-MOF, ZnO/MOF25 and ZnO/MOF50 samples.

Fig. 11 shows the PL emission for all samples at room temperature under an excitation of 350.7 nm, where broad band profiles can be seen covering all the visible spectrum. The PL emission band profile is typical of a multiphonon process, where relaxation occurs by different paths involving several energy states within the band gap [61,62]. The emission in the visible blue region can be attributed to the intrinsic defects, and in contrast, the red emission can be related with the extrinsic defects, this typical behavior was reported in previous work [33,34]. The difference between the ZnO PL behavior synthesized in this work compared to those obtained in previous works [33,34] is that in this case the presence of a single emission broad band is observed and in

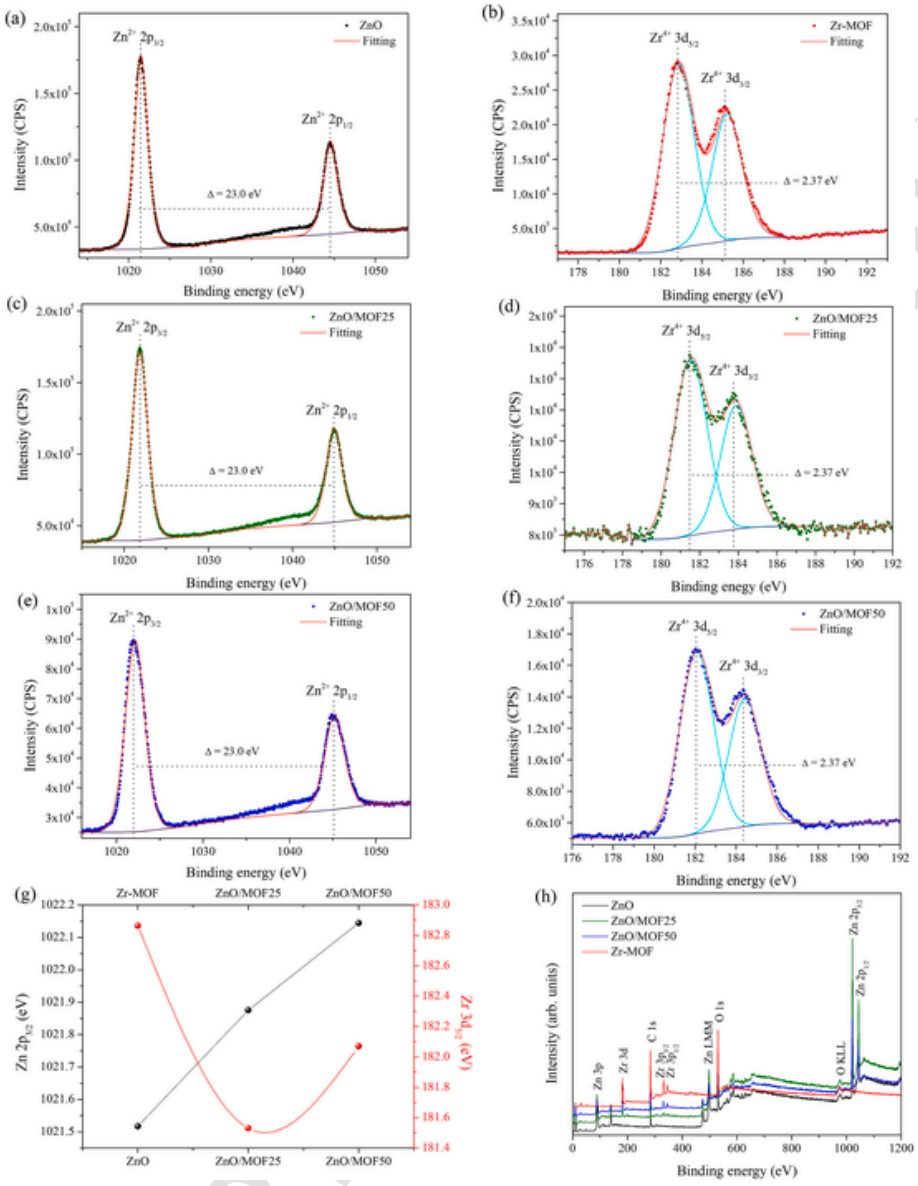

Fig. 7. Peak-differentiating-imitating analysis of XPS spectra of Zn 2*p* for ZnO (a), ZnO/MOF25 (b), and ZnO/MOF50 (c), and of Zr 3*d* for Zr-MOF (d), ZnO/MOF25 (e), and ZnO/MOF50 (f). Zn $2p_{3/2}$ and Zr $3d_{5/2}$ energy values, and survey spectra for all samples.

the other cases, two emission bands were observed. This fact can be attributed to the change in the synthesis method.

Fig. 11 (f)–(i) show the Zr-MOF concentration dependence on PL emission, where an increase in the luminescence intensity can be observed with the increase in the Zr-MOF amount. The PL intensity of the ZnO, Zr-MOF and ZnO/MOF25 samples was similar. However, it strongly increased with the introduction of 50 wt% Zr-MOF. A variety of factors can influence the PL intensity, such as morphology, particle size, synthesis method, calcination temperature and number of oxygen vacancies, among others [63,64]. According to the literature, the PL behavior are directly linked to the structural order-disorder of the lattice, indicating that the increase in the intensity of PL emission requires some simultaneous order-disorder in the system and that totally disordered or highly crystalline structures lead to reduced PL emission [62].

The PL spectrum peak of all samples was deconvoluted using the PickFit program with the Voigt area function, as shown in Fig. 11(b–g). The PL deconvolution results revealed four emission peaks at 492.3 nm (blue), 536.7 nm (yellow), 586.8 nm (green) and 637.7 nm (red) for all samples. Analyzing the spectra, an increase in the red emission was observed. As aforementioned, many factors influence the PL intensity; in addition, the red emission was found to be extrinsic and possibly defect-related. According to this, the FEG-SEM, Raman, BET, UV–vis and XPS analyses indicated significant changes in the morphology, structure, particle size, band gap states and concentration of oxygen vacancies of the ZnO/MOF50 sample, suggesting that this system became more disordered. In this way, the increase in the luminescence intensity accompanied by an increase in the emission in the red region of the spectrum observed in the ZnO/MOF50 sample can be attributed to the fact that structural defects can facilitate the accommodation of electrons in different energy states, thus increasing radioactive recombination. After the analysis of these results it was expected that the ZnO/MOF50 sample presented a worsening of its photoelectrochemical properties.

Fig. 12 shows the linear sweep voltammetry curves for all samples both in the dark and light conditions.

The J-V characteristics of the developed photoanode were analyzed in the potential range of 0.6–2 V in an I_3^-/I^- solution, commonly used as a standard electrolyte in the construction of a DSSC, at 20 mV s^{-1}.

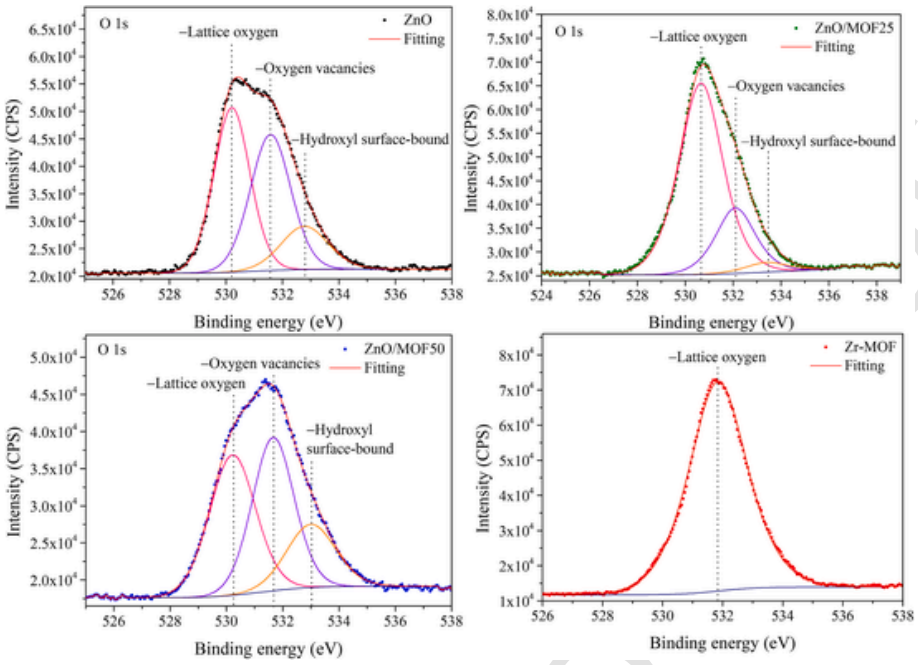

Fig. 8. Peak-differentiating-imitating analysis of O 1*s* XPS spectra for ZnO (a), ZnO/MOF25 (b), ZnO/MOF50 (c), and Zr-MOF (d).

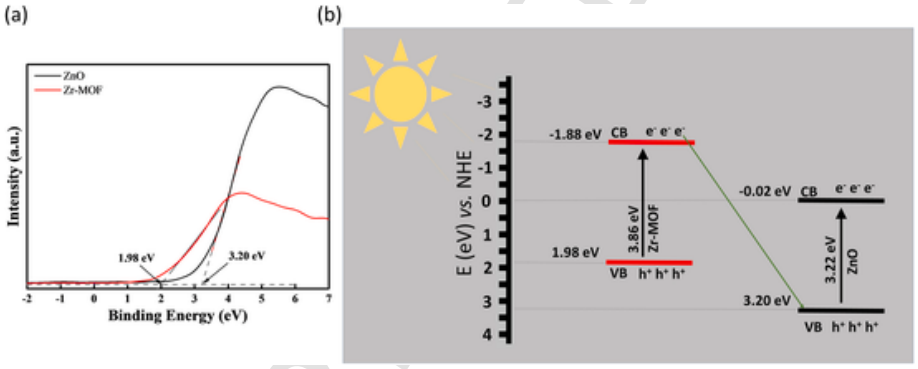

Fig. 9. VB-XPS spectra of ZnO and Zr-MOF samples (a) and energy band diagram of the ZnO/MOF composite (b).

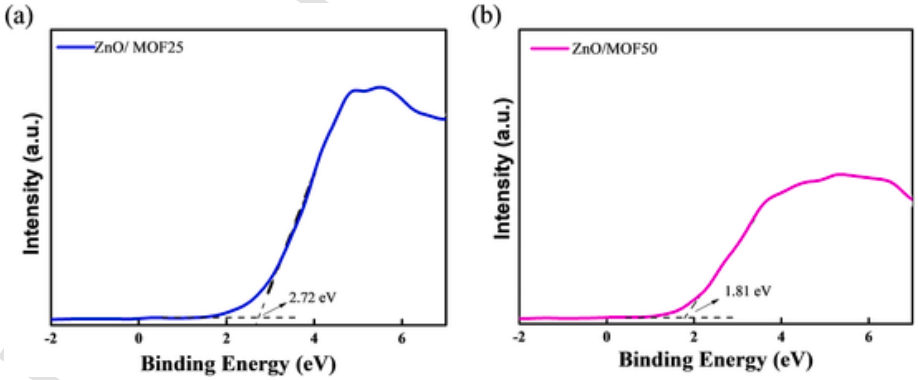

Fig. 10. VB-XPS spectra result of ZnO/MOF25 (a) and ZnO/MOF50 (b).

This result shows a semiconducting behavior of the developed ZnO/MOF photoanodes, which is a desired property in the fabrication of DSSCs. It was also evident that the introduction of 25 wt% Zr-MOF into the ZnO particle significantly improved the charge transfer characteristics compared to the pure ZnO and ZnO/MOF50 samples. The sample with 50 wt% Zr-MOF (ZnO/MOF50) presented a current density lower than that with 25 wt% Zr-MOF, indicating that 50 wt% is an excessive amount responsible for reducing the active sites and slowing the diffusion process for the electrolyte. It could also be observed that the current density increased under light conditions in all samples. The ZnO, ZnO/MOF25 and ZnO/MOF50 samples presented a current density of 2.02, 4.12 and 2.95 mA cm^{-2}, respectively, at 1.2 V in the presence of light. This indicates that the addition of 25 wt% Zr-MOF almost doubled the current density of the pristine ZnO film under light condition,

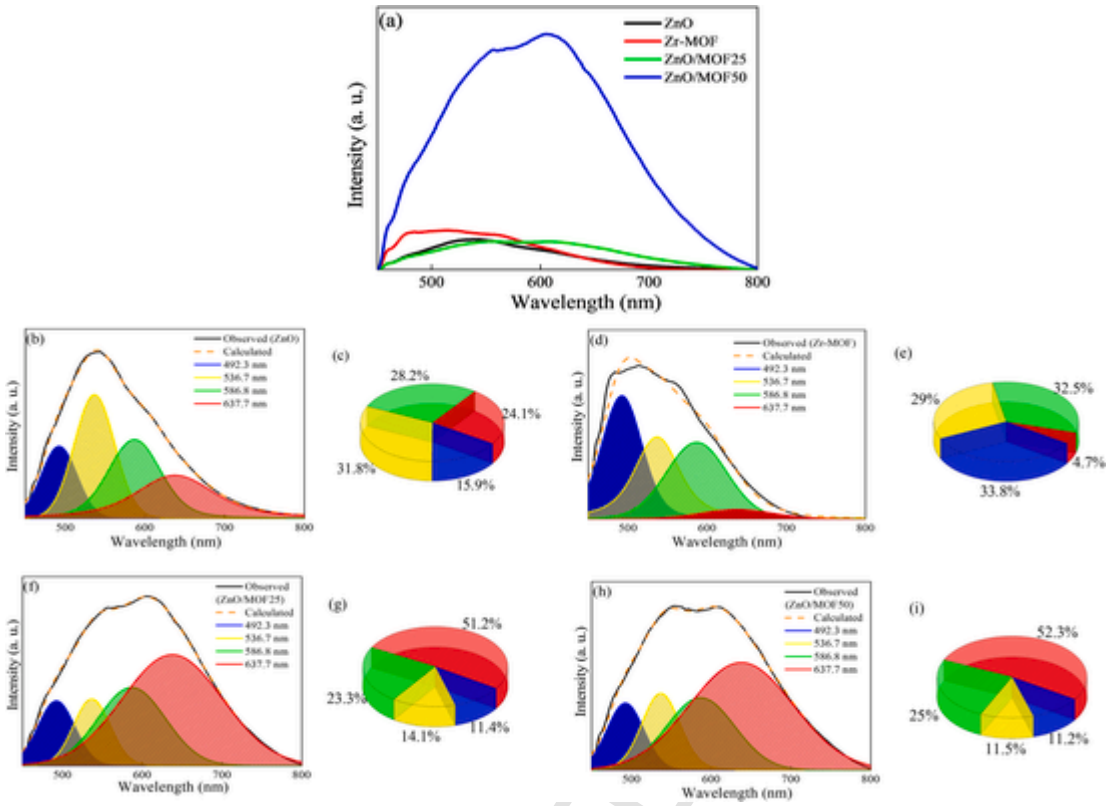

Fig. 11. PL spectra (a) and deconvolution of the spectra and percentage of each area deconvoluted for ZnO (b–c), Zr-MOF (d–e), ZnO/MOF25 (f–g) and ZnO/MOF50 (h–i) particles at room temperature.

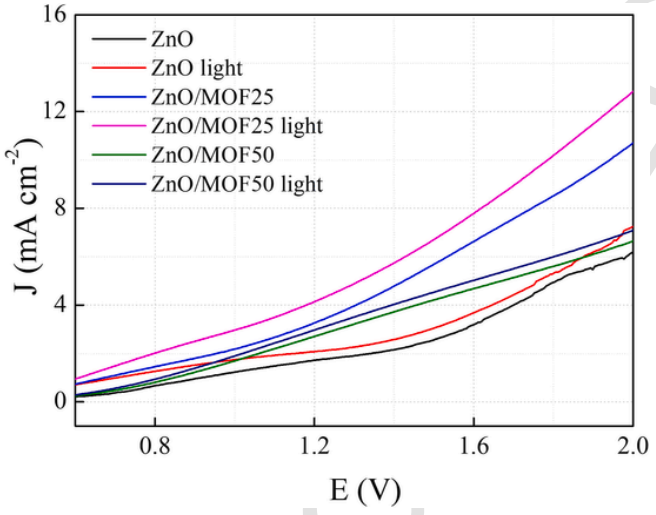

Fig. 12. Linear sweep voltammetry curves of the ZnO, Zr-MOF, ZnO/MOF25 and ZnO/MOF50 samples at 20 mV s^{-1}.

which is a promising result for the manufacture of solar cell photoanodes.

4. Conclusion

The ZnO flower-type structure was modified with the addition of Zr-MOF by mechanical mixture followed by heat treatment. ZnO/MOF samples with two different amounts of Zr-MOF were structurally and morphologically characterized. The characterizations revealed the heterostructure formation between the ZnO and Zr-MOF. The FEG-SEM results showed that the morphology of ZnO changes from flower-type structure to cross-linked multileveled porous nanoflowers with the addition of Zr-MOF. The comparison between the ZnO, Zr-MOF and ZnO/Zr-MOF photoanodes evidenced that the electrode with 25 wt% Zr-MOF improves the charge transfer characteristics. On the other hand, as expected, the sample with 50 wt% Zr-MOF (ZnO/MOF50) showed that an excessive amount of Zr-MOF into ZnO tends to reduce the active sites and slow the diffusion process for the electrolyte. In conclusion, the results revealed that the modification of ZnO with the addition of Zr-MOF has the ability to enhance charge transport and inhibit charge recombination, proving to be an interesting material for the manufacture of solar cell photoanodes.

CRediT authorship contribution statement

Letícia G. da Trindade: Conceptualization, Investigation, Writing - original draft. **Katiúscia M.N. Borba:** Investigation. **Aline B. Trench:** Investigation. **Letícia Zanchet:** Investigation. **Vinícius Teodoro:** Investigation. **Fenelon M.L. Pontes:** Writing - review & editing. **Elson Longo:** Resources. **Tatiana M. Mazzo:** Supervision, Writing - original draft.

Declaration of competing interest

The authors declare that they have no known competing financial interests or personal relationships that could have appeared to influence the work reported in this paper.

Acknowledgments

The authors appreciate the support of the Brazilian research financing institutions: Coordenação de Aperfeiçoamento de Pessoal de Nível Superior - Brasil (CAPES) - Finance Code 001, São Paulo Research Foundation – FAPESP (2013/07296-2) and Conselho Nacional de Desenvolvimento Científico e Tecnológico.

Appendix A. Supplementary data

Supplementary data related to this article can be found at https://doi.org/10.1016/j.jssc.2020.121794.

Data availability

The raw/processed data required to reproduce these findings cannot be shared at this time due to technical or time limitations.

Uncited references

[54].

References

[1] H. Saleem, W. Jiandong, K. Zaman, E.E. Elashkar, A.M. Shoukry, The impact of air-railways transportation, energy demand, bilateral aid flows, and population density on environmental degradation: evidence from a panel of next-11 countries, Transp Res D Transp Environ 62 (2018) 152–168, doi:10.1016/j.trd.2018.02.016.

[2] K. Dong, G. Hochman, Y. Zhang, R. Sun, H. Li, H. Liao, CO_2 emissions, economic and population growth, and renewable energy: empirical evidence across regions, Energy Econ. 75 (2018) 180–192, doi:10.1016/j.eneco.2018.08.017.

[3] S. Guo, Q. Liu, J. Sun, H. Jin, A review on the utilization of hybrid renewable energy, Renew. Sustain. Energy Rev. 91 (2018) 1121–1147, doi:10.1016/j.rser.2018.04.105.

[4] V. Indragandhi, R. Logesh, V. Subramaniyaswamy, V. Vijayakumar, P. Siarry, L. Uden, Multi-objective optimization and energy management in renewable based AC/DC microgrid, Comput. Electr. Eng. 70 (2018) 179–198, doi:10.1016/j.compeleceng.2018.01.023.

[5] G. Schwerhoff, M. Sy, Financing renewable energy in Africa – key challenge of the sustainable development goals, Renew. Sustain. Energy Rev. 75 (2017) 393–401, doi:10.1016/j.rser.2016.11.004.

[6] G.L. Kyriakopoulos, G. Arabatzis, Electrical energy storage systems in electricity generation: energy policies, innovative technologies, and regulatory regimes, Renew. Sustain. Energy Rev. 56 (2016) 1044–1067, doi:10.1016/j.rser.2015.12.046.

[7] S. Mahalingam, H. Abdullah, Electron transport study of indium oxide as photoanode in DSSCs: a review, Renew. Sustain. Energy Rev. 63 (2016) 245–255, doi:10.1016/j.rser.2016.05.067.

[8] K. Ahmad, A. Mohammad, S.M. Mobin, Hydrothermally grown α-MnO2 nanorods as highly efficient low cost counter-electrode material for dye-sensitized solar cells and electrochemical sensing applications, Electrochim. Acta 252 (2017) 549–557, doi:10.1016/j.electacta.2017.09.010.

[9] L. Chen, W. Chen, E. Wang, Graphene with cobalt oxide and tungsten carbide as a low-cost counter electrode catalyst applied in Pt-free dye-sensitized solar cells, J. Power Sources 380 (2018) 18–25, doi:10.1016/j.jpowsour.2017.11.057.

[10] A. Bora, K. Mohan, P. Phukan, S.K. Dolui, A low cost carbon black/polyaniline nanotube composite as efficient electro-catalyst for triiodide reduction in dye sensitized solar cells, Electrochim. Acta 259 (2018) 233–244, doi:10.1016/j.electacta.2017.10.156.

[11] N.A. Karim, U. Mehmood, H.F. Zahid, T. Asif, Nanostructured photoanode and counter electrode materials for efficient Dye-Sensitized Solar Cells (DSSCs), Sol. Energy 185 (2019) 165–188, doi:10.1016/j.solener.2019.04.057.

[12] J. Gonga, K. Sumathy, Q. Qiao, Z. Zhou, Review on dye-sensitized solar cells (DSSCs): advanced techniques and research trends, Renew. Sustain. Energy Rev. 68 (2017) 234–246, doi:10.1016/j.rser.2016.09.097.

[13] P. Selvaraj, H. Baig, T.K. Mallick, J. Siviter, A. Montecucco, W. Li, M. Paul, T. Sweet, M. Gao, A.R. Knox, S. Sundaram, Enhancing the efficiency of transparent dye-sensitized solar cells using concentrated light, Sol. Energy Mater. Sol. Cells 175 (2018) 29–34, doi:10.1016/j.solmat.2017.10.006.

[14] H. Bashar, M.M.H. Bhuiyan, M.R. Hossain, F. Kabir, M.S. Rahaman, M.S. Manir, T. Ikegami, Study on combination of natural red and green dyes to improve the power conversion efficiency of dye sensitized solar cells, Optik (2019) 620–625, doi:10.1016/j.ijleo.2019.03.043.

[15] J. Luo, Y. Wang, Q. Zhang, Progress in perovskite solar cells based on ZnO nanostructures, Sol. Energy 163 (2018) 289–306, doi:10.1016/j.solener.2018.01.035.

[16] S. Aksoy, K. Gorgun, Y. Caglar, M. Caglar, Effect of loading and standbye time of the organic dye N719 on the photovoltaic performance of ZnO based DSSC, J. Mol. Struct. 1189 (2019) 181–186, doi:10.1016/j.molstruc.2019.04.040.

[17] A.P. Uthirakumar, Fabrication of ZnO Based Dye Sensitized Solar Cells, InTech, 2011, doi:10.5772/19459.

[18] J. Dong, Y. Zhao, J. Shi, H. Wei, J. Xiao, X. Xu, J. Luo, J. Xu, D. Li, Y. Luo, Q. Meng, Impressive enhancement in the cell performance of ZnO nanorod-based perovskite solar cells with Al-doped ZnO interfacial modification, Chem. Commun. 50 (2014) 13381–13384.

[19] C. Li, Z. Zang, C. Han, Z. Hu, X. Tang, J. Du, Y. Leng, K. Sun, Highly compact CsPbBr3 perovskite thin films decorated by ZnO nanoparticles for enhanced random lasing, Nanomater. Energy 40 (2017) 195–202, doi:10.1016/j.nanoen.2017.08.013.

[20] H. Wang, S. Cao, B. Yang, H. Li, M. Wang, X. Hu, K. Sun, Z. Zang, NH_4Cl-Modified ZnO for high-performance $CsPbIBr_2$ perovskite solar cells via low-temperature process, Sol RRL 4 (2019) 1900363, doi:10.1002/solr.201900363.

[21] S. Cao, H. Wang, H. Li, J. Chen, Z. Zang, Critical role of interface contact modulation in realizing low-temperature fabrication of efficient and stable $CsPbIBr_2$ perovskite solar cells, Chem. Eng. J. 394 (2020) 124903, doi:10.1016/j.cej.2020.124903.

[22] H. Wang, P. Zhang, Z. Zang, High performance $CsPbBr_3$ quantum dots photodetectors by using zinc oxide nanorods arrays as an electron-transport layer, Appl. Phys. Lett. 116 (2020) 162103, doi:10.1063/5.0005464.

[23] J. Chou, C. Ko, P. Kuo, C. Lai, Y. Nien, J. Chang, Fabrication of dye-sensitized solar cells using zinc oxide nanorod-modified titanium dioxide photoanode, IEEE Trans. Nanotechnol. 18 (2019) 553–561, doi:10.1109/TNANO.2019.2915367.

[24] M. Zhong, L. Chai, Y. Wang, Core-shell structure of ZnO@TiO2 nanorod arrays as electron transport layer for perovskite solar cell with enhanced efficiency and stability, Appl. Surf. Sci. 464 (2019) 301–310, doi:10.1016/j.apsusc.2018.09.080.

[25] S. Zhuang, M. Lu, N. Zhou, L. Zhou, D. Lin, Z. Peng, Q. Wu, Cu modified ZnO nanoflowers as photoanode material for highly efficient dye sensitized solar cells, Electrochim. Acta 294 (2019) 28–37, doi:10.1016/j.electacta.2018.10.045.

[26] Y. Li, H. Xu, S. Ouyang, J. Ye, Metal–organic frameworks for photocatalysis, Phys. Chem. Chem. Phys. 18 (2016) 7563–7572, doi:10.1039/C5CP05885F.

[27] C. Bao, L. Zhou, Y. Shao, Q. Wu, H. Zhu, K. Li, A novel Au-loaded magnetic metal organic framework/graphene multifunctional composite: green synthesis and catalytic application, J. Ind. Eng. Chem. 38 (2016) 132–140, doi:10.1016/j.jiec.2016.04.014.

[28] H. Liu, X. Ren, L. Chen, Synthesis and characterization of magnetic metal–organic framework for the adsorptive removal of Rhodamine B from aqueous solution, J. Ind. Eng. Chem. 34 (2016) 278–285, doi:10.1016/j.jiec.2015.11.020.

[29] R. Kaur, A.L. Sharma, K.-H. Kim, A. Deep, A novel CdTe/Eu-MOF photoanode for application in quantum dot sensitized solar cell to improve power conversion efficiency, J. Ind. Eng. Chem. 53 (2017) 77–81, doi:10.1016/j.jiec.2017.04.002.

[30] R. Kaur, K.-H. Kim, A.K. Paul, A. Deep, Recent advances in the photovoltaic applications of coordination polymers and metal organic frameworks, J. Mater. Chem. 4 (2016) 3991–4002, doi:10.1039/C5TA09668E.

[31] J. Dou, Y. Li, F. Xie, X. Ding, M. Wei, Metal–organic framework derived hierarchical porous anatase TiO_2 as a photoanode for dye-sensitized solar cell, Cryst. Growth Des. 161 (2016) 121–125, doi:10.1021/acs.cgd.5b01003.

[32] C.-C. Lee, C.-I. Chen, Y.-T. Liao, K.C.-W. Wu, C.-C. Chueh, Enhancing efficiency and stability of photovoltaic cells by using perovskite/Zr-MOF heterojunction including bilayer and hybrid structures, Adv. Sci. 6 (2019) 1801715, doi:10.1002/advs.201801715.

[33] L.G. da Trindade, G.B. Minervino, A.B. Trench, M.H. Carvalho, M. Assis, M.S. Li, A.J.A. de Oliveira, E.C. Pereira, T.M. Mazzo, E. Longo, Influence of ionic liquid on the photoelectrochemical properties of ZnO particles, Ceram. Int. 44 (2018) 10393–10401, doi:10.1016/j.ceramint.2018.03.053.

[34] L.G. da Trindade, G.Y. Hata, J.C. Souza, M.R.S. Soares, E.R. Leite, E.C. Pereira, E. Longo, T.M. Mazzo, Preparation and characterization of hematite nanoparticles-decorated zinc oxide particles (ZnO/Fe_2O_3) as photoelectrodes for solar cell applications, J. Mater. Sci. 55 (2020) 2923–2936, doi:10.1007/s10853-019-04135-x.

[35] A. Ghorbanpour, L.D. Huelsenbeck, D.-M. Smilgies, G. Giri, Oriented UiO-66 thin films through solution shearing, CrystEngComm 20 (2018) 294–300, doi:10.1039/C7CE01801K.

[36] L.G. da Trindade, K.M.N. Borba, L. Zanchet, D.W. Lima, A.B. Trench, F. Rey, U. Diaz, E. Longo, K. Bernardo-Gusmão, E.M.A. Martini, SPEEK-based proton exchange membranes modified with MOF-encapsulated ionic liquid, Mater. Chem. Phys. 236 (2019) 121792, doi:10.1016/j.matchemphys.2019.121792.

[37] Y. Zhang, J. Guo, L. Shi, Y. Zhu, K. Hou, Y. Zheng, Z. Tang, Tunable chiral metal organic frameworks toward visible light–driven asymmetric catalysis, Sci. Adv. 3 (2017) e1701162, doi:10.1126/sciadv.1701162.

[38] A. Chen, Q. Su, H. Han, E. Enriquez, Q. Jia, Metal oxide nanocomposites: a perspective from strain, defect, and interface, Adv. Mater. 31 (2019) 1803241, doi:10.1002/adma.201803241.

[39] M. Yadav, V. Singh, Y.C. Sharma, Methyl transesterification of waste cooking oil using a laboratory synthesized reusable heterogeneous base catalyst: process optimization and homogeneity study of catalyst, Energy Convers. Manag. 148 (2017) 1438–1452, doi:10.1016/j.enconman.2017.06.024.

[40] I.D. Ivanchikova, J.S. Lee, N.V. Maksimchuk, A.N. Shmakov, Y.A. Chesalov, A.B. Ayupov, Y.K. Hwang, C.-H. Jun, J.-S. Chang, O.A. Kholdeeva, Highly selective H_2O_2-based oxidation of alkylphenols to p-benzoquinones over MIL-125 metal-organic frameworks, Eur. J. Inorg. Chem. (1) (2014) 132–139, doi:10.1002/ejic.201301098.

[41] L.G. da Trindade, L. Zanchet, R. Dreon, J.C. Souza, M. Assis, E. Longo, E.M.A. Martini, A.J. Chiquito, F.M. Pontes, Microwave-assisted solvothermal preparation of Zr-BDC for modification of proton exchange membranes made of SPEEK/PBI blends, J. Mater. Sci. (2020), doi:10.1007/s10853-020-05068-6.

[42] Y. Han, M. Liu, K. Li, Y. Zuo, Y. Wei, S. Xu, G. Zhang, C. Song, Z. Zhang, X. Guo, Facile synthesis of morphology and sizecontrolled zirconium metal–organic framework UiO-66: the role of hydrofluoric acid in crystallization, CrystEngComm 17 (2015) 6434–6440, doi:10.1039/c5ce00729a.

[43] M. Rajalakshmi, A.K. Arora, B.S. Bendre, S. Mahamuni, Optical phonon confinement in zinc oxide nanoparticles, J. Appl. Phys. 87 (2000) 2445–2448, doi:10.1063/1.372199.

[44] R. Cuscó, E. Alarcón-Lladó, J. Ibáñez, L. Artús, J. Jiménez, B. Wang, M.J. Callahan, Temperature dependence of Raman scattering in ZnO, Phys. Rev. B 75 (2007) 165202, doi:10.1103/PhysRevB.75.165202.
[45] K.A. Alim, V.A. Fonoberov, A.A. Balandin, Origin of the optical phonon frequency shifts in ZnO quantum dots, Appl. Phys. Lett. 86 (2005) 53103-3 053103, doi:10.1063/1.1861509.
[46] P. Wang, G. Xu, P. Jin, Size dependence of electron-phonon coupling in ZnO nanowires, Phys. Rev. B 69 (2004) 113303, doi:10.1103/PhysRevB.69.113303.
[47] L. Maschio, B. Kirtman, M. Rérat, R. Orlando, R. Dovesi, Ab initio analytical Raman intensities for periodic systems through a coupled perturbed Hartree-Fock/Kohn-Sham method in an atomic orbital basis. II. Validation and comparison with experiments, J. Chem. Phys. 139 (2013) 164102, doi:10.1063/1.4824443.
[48] L.G. da Trindade, L. Zanchet, A.B. Trench, J.C. Souza, M.H. Carvalho, A.J.A. de Oliveira, E.C. Pereira, T.M. Mazzo, E. Longo, Flower-like ZnO/ionic liquid composites: structure, morphology, and photocatalytic activity, Ionics 25 (2019) 3197–3210, doi:10.1007/s11581-018-2822-x.
[49] V.V. Butova, K.S. Vetlitsyna-Novikova, I.A. Pankin, K.M. Charykov, A.L. Trigub, A.V. Soldatov, Microwave synthesis and phase transition in UiO-66/MIL-140A system, Microporous Mesoporous Mater. 296 (2020) 109998, doi:10.1016/j.micromeso.2020.109998.
[50] S. Yi, F. Zhao, X. Yue, D. Wang, Y. Lin, Enhanced solar light-driven photocatalytic activity of BiOBr–ZnO heterojunctions with effective separation and transfer properties of photo-generated chargers, New J. Chem. 39 (2015) 6659–6666, doi:10.1039/C5NJ00707K.
[51] T.T. Ngo, Photocatalytic Reduction of CO2 with Tunable Bandgap and Bandedge Materials, Graduate Theses and Dissertations, 2016. http://scholarcommons.usf.edu/etd/6551.
[52] V. Ramasubbu, P.R. Kumar, E.M. Mothi, K. Karuppasamy, H.-S. Kim, T. Maiyalagan, X.S. Shajan, Highly interconnected porous TiO2-Ni-MOF composite aerogel photoanodes for high power conversion efficiency in quasi-solid dye-sensitized solar cells, Appl. Surf. Sci. 496 (2019) 143646, doi:10.1016/j.apsusc.2019.143646.
[53] P. Periyat, K.V. Baiju, P. Mukundan, P.K. Pillai, K.G.K. Warrier, Aqueous colloidal sol–gel route to synthesize nanosized ceria-doped titania having high surface area and increased anatase phase stability, J. Sol. Gel Sci. Technol. 43 (2007) 299–304, doi:10.1007/s10971-007-1583-1.
[54] A. Kumara, S. Mondal, K.S.R.K. Rao, Experimental evidences of charge transition levels in ZrO_2 and at the Si: ZrO_2 interface by deep level transient spectroscopy, Appl. Phys. Lett. 110 (2017) 132904, doi:10.1063/1.4979522.
[55] R. Al-Gaashani, S. Radiman, A.R. Daud, N. Tabet, Y. Al-Douri, XPS and optical studies of different morphologies of ZnO nanostructures prepared by microwave methods, Ceram. Int. 39 (2013) 2283–2292, doi:10.1016/j.ceramint.2012.08.075.
[56] J. Xu, S. He, H. Zhang, J. Huang, H. Lin, X. Wang, J. Long, Layered metal–organic framework/graphene nanoarchitectures for organic photosynthesis under visible light, J. Mater. Chem. 3 (2015) 24261–24271, doi:10.1039/C5TA06838J.
[57] L.-L. Qian, Z.-X. Wang, L.-M. Zhu, K. Li, B.-L. Li, B. Wu, Synthesis, structure, spectral characteristic and photocatalytic degradation of organic dyes of a copper metal-organic framework based on tri(triazole) and pimelate, Spectrochim. Acta Mol. Biomol. Spectrosc. 214 (2019) 372–377, doi:10.1016/j.saa.2019.02.059.
[58] V. Etacheri, C. Di Valentin, J. Schneider, D. Bahnemann, S.C. Pillai, Visible light activation of TiO_2 photocatalysts: advances in theory and experiments, J. Photochem. Photobiol., A C 25 (2015) 1–29, doi:10.1016/j.jphotochemrev.2015.08.003.
[59] J. He, J. Wang, Y. Chen, J. Zhang, D. Duan, Y. Wang, Z. Yan, A dye-sensitized Pt@UiO-66(Zr) metal–organic framework for visible-light photocatalytic hydrogen production, Chem. Commun. 50 (2014) 7063–7066, doi:10.1039/C4CC01086H.
[60] C.F. Lin, C.H. Kao, C.Y. Lin, Y.W. Liu, C.H. Wang, The electrical and physical characteristics of Mg-doped ZnO sensing membrane in EIS (electrolyte–insulator–semiconductor) for glucose sensing applications, Results Phys 16 (2020) 102976, doi:10.1016/j.rinp.2020.102976.
[61] L.S. Cavalcante, M.A. Almeida, W. Avansi Jr., R.L. Tranquilin, E. Longo, N.C. Batista, V.R. Mastelaro, M.S. Li, Cluster coordination and photoluminescence properties of α-Ag_2WO_4 microcrystals, Inorg. Chem. 51 (2012) 10675–10687, doi:10.1021/ic300948n.
[62] V.M. Longo, E. Orhan, L.S. Cavalcante, S.L. Porto, J.W.M. Espinosa, J.A. Varela, E. Longo, Understanding the origin of photoluminescence in disordered Ca 0.60Sr 0.40WO 4: an experimental and first-principles study, Chem. Phys. 334 (2007) 180–188, doi:10.1016/j.chemphys.2007.02.025.
[63] Z. Amouzegar, R. Naghizadeh, H.R. Rezaie, M. Ghahari, M. Aminzare, Cubic $ZnWO_4$ nano-photocatalysts synthesized by the microwave-assisted precipitation technique, Ceram. Int. 41 (2015) 8352–8359, doi:10.1016/j.ceramint.2014.09.119.
[64] A.A. Blistanov, B.I. Zadneprovski, M.A. Ivanov, V.V. Kochurikhin, V.S. Petrakov, I.O. Yakimova, Luminescence of crystals of divalent tungstates, Crystallogr. Rep. 50 (2005) 284–290, doi:10.1134/1.1887903.